nature astronomy

LETTERS

https://doi.org/10.1038/s41550-018-0420-5

An Earth-sized exoplanet with a Mercury-like composition

A. Santerne[1*], B. Brugger[1], D. J. Armstrong[2], V. Adibekyan[3], J. Lillo-Box[4], H. Gosselin[1,5], A. Aguichine[1,6], J.-M. Almenara[7], D. Barrado[8], S. C. C. Barros[3], D. Bayliss[7], I. Boisse[1], A. S. Bonomo[9], F. Bouchy[7], D. J. A. Brown[2], M. Deleuil[1], E. Delgado Mena[3], O. Demangeon[3], R. F. Díaz[7,10,11], A. Doyle[2], X. Dumusque[7], F. Faedi[2,12], J. P. Faria[3,13], P. Figueira[3,4], E. Foxell[2], H. Giles[7], G. Hébrard[14,15], S. Hojjatpanah[3,13], M. Hobson[1], J. Jackman[2], G. King[2], J. Kirk[2], K. W. F. Lam[2], R. Ligi[1], C. Lovis[7], T. Louden[2], J. McCormac[2], O. Mousis[1], J. J. Neal[3,13], H. P. Osborn[1,2], F. Pepe[7], D. Pollacco[2], N. C. Santos[3,13], S. G. Sousa[3], S. Udry[7] and A. Vigan[1]

Earth, Venus, Mars and some extrasolar terrestrial planets[1] have a mass and radius that is consistent with a mass fraction of about 30% metallic core and 70% silicate mantle[2]. At the inner frontier of the Solar System, Mercury has a completely different composition, with a mass fraction of about 70% metallic core and 30% silicate mantle[3]. Several formation or evolution scenarios are proposed to explain this metal-rich composition, such as a giant impact[4], mantle evaporation[5] or the depletion of silicate at the inner edge of the protoplanetary disk[6]. These scenarios are still strongly debated. Here, we report the discovery of a multiple transiting planetary system (K2-229) in which the inner planet has a radius of 1.165 ± 0.066 Earth radii and a mass of 2.59 ± 0.43 Earth masses. This Earth-sized planet thus has a core-mass fraction that is compatible with that of Mercury, although it was expected to be similar to that of Earth based on host-star chemistry[7]. This larger Mercury analogue either formed with a very peculiar composition or has evolved, for example, by losing part of its mantle. Further characterization of Mercury-like exoplanets such as K2-229 b will help to put the detailed in situ observations of Mercury (with MESSENGER and BepiColombo[8]) into the global context of the formation and evolution of solar and extrasolar terrestrial planets.

The star EPIC 228801451 (TYC 4947-834-1; 2MASS J12272958-0643188; K2-229) was observed in photometry as part of campaign 10 of the K2 mission with the Kepler space telescope, from 2016 July 6 to 2016 September 20 with a 30 min cadence. Analysis of the extracted and reduced light curve using the POLAR (Planet candidates from OptimaL Aperture Reduction) pipeline[9] revealed two sets of periodic planetary transit-like events on periods of about 14 h and 8.3 d. A single transit-like event near the mid-campaign time was also detected (see Fig. 1 and Methods). We refer to these planets as K2-229 b, c and d, respectively. The light curve exhibits a large modulation with a 2% peak-to-peak amplitude and 18 d period variability (see Fig. 1) that is caused by the presence of active regions (spots and/or faculae). The star is a bright (magnitude in the visual wavelength band $V = 11$ mag, following the Vega magnitude system) late-G/early-K dwarf[10], and hence is suitable for precise radial velocity (RV) observations.

We observed EPIC 228801451 with the HARPS (High Accuracy Radial velocity Planet Searcher) spectrograph with the aim of confirming the planetary nature of the transiting candidates and measuring the mass through Doppler spectroscopy. We collected 120 RVs from 2017 January 26 to 2017 May 4 with up to four observations each night. We reduced the spectra using the online pipeline available at the telescope and derived the RV, the full-width at half-maximum (FWHM) and the bisector (BIS) of the averaged line profile, as well as the spectroscopic indices of chromospheric activity in the core of five spectral lines (see Methods and Supplementary Tables 3 and 4). The pipeline automatically rejected one poor-quality spectrum.

To assess the planetary nature of the detected transit signals and rule out the presence of background stellar objects contaminating the light curve, we performed high-resolution imaging observations with the AstraLux lucky-imaging instrument. No background or stellar companion is detected within the sensitivity limits of the data and within the photometric mask (see Methods and Supplementary Fig. 2).

We co-added the HARPS spectra and derived the spectral parameters of the host star[11] (see Methods). We find that the host star has an effective temperature $T_{\rm eff} = 5{,}120 \pm 39$ K, a surface gravity $\log g = 4.51 \pm 0.12$, an iron/hydrogen abundance ratio $[{\rm Fe/H}] = -0.06 \pm 0.02$ decimal exponents (dex), where the square brackets indicate that the ratio is the log relative to solar values, and a microturbulence velocity $v_{\rm mic} = 0.74 \pm 0.08\,{\rm km\,s^{-1}}$. This identifies the host

[1]Aix Marseille Univ., CNRS, LAM, Laboratoire d'Astrophysique de Marseille, Marseille, France. [2]Department of Physics, University of Warwick, Coventry, UK. [3]Instituto de Astrofísica e Ciências do Espaço, Universidade do Porto, CAUP, Porto, Portugal. [4]European Southern Observatory (ESO), Santiago de Chile, Chile. [5]Université de Toulouse, UPS-OMP, IRAP, Toulouse, France. [6]Paris-Saclay Université, ENS Cachan, Cachan, France. [7]Observatoire Astronomique de l'Université de Genève, Versoix, Switzerland. [8]Depto. de Astrofísica, Centro de Astrobiología (CSIC-INTA), Madrid, Spain. [9]INAF—Osservatorio Astrofisico di Torino, Pino Torinese, Italy. [10]Universidad de Buenos Aires, Facultad de Ciencias Exactas y Naturales, Buenos Aires, Argentina. [11]CONICET—Universidad de Buenos Aires, Instituto de Astronomía y Física del Espacio (IAFE), Buenos Aires, Argentina. [12]INAF—Osservatorio Atrofisico di Catania, Catania, Italy. [13]Departamento de Física e Astronomia, Faculdade de Ciencias, Universidade do Porto, Porto, Portugal. [14]Institut d'Astrophysique de Paris, UMR7095 CNRS, Universite Pierre & Marie Curie, Paris, France. [15]Aix Marseille Univ., CNRS, OHP, Observatoire de Haute Provence, Saint Michel l'Observatoire, France. *e-mail: alexandre.santerne@lam.fr

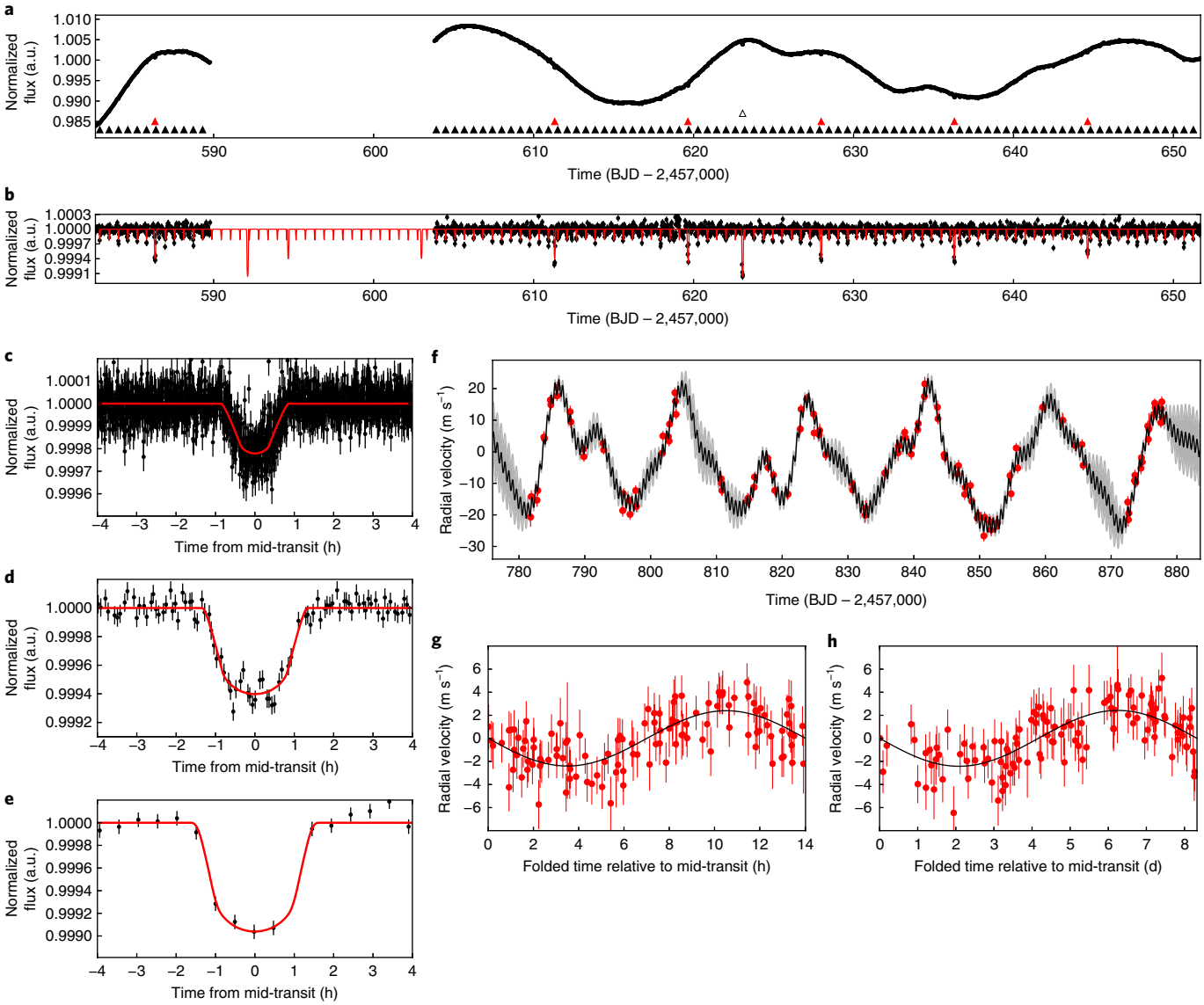

Fig. 1 | Photometric and RV data of the K2-229 system. a, Extracted and normalized K2 light curve. The times of transit (in units of barycentric Julian date (BJD) minus 2,457,000) of the planets b, c and d are indicated by the black, red and white triangles, respectively. **b**, Gaussian process flattened light curve (in black) with the best three-planet photometric model (red line). **c**–**e**, Phase-folded transit light curves (in black) of the planets b, c and d, respectively. The best transit model is displayed in red. **f**, RV time series obtained with HARPS (in red) together with the best three-Keplerian orbit and a Gaussian process regression (in black). The grey region corresponds to the 68.3% credible interval from the Gaussian process. **g**,**h**, Time-folded RV data (in red) to the transit epoch and period of the planets b and c, respectively. The data are corrected from the activity signals and the other planetary contribution. The best Keplerian orbit models are shown in black. Error bars are confidence intervals.

star as a K0 dwarf. We also derived the chemical abundance of the star (see Supplementary Table 2).

The 119-RV time series is displayed in Fig. 1 and exhibits a large variability at the level of about 50 m s^{-1} and a recurrence timescale of 18 d. This large modulation is not caused by planet reflex motions, but is due to the presence of active regions on the surface of the star[12]. We performed a joint analysis of the photometric and spectroscopic data, together with the spectral energy distribution (SED) of the star with PASTIS (Planet Analysis and Small Transit Investigation Software)[13] (see Methods). We used three different approaches to correct the RV data for the activity signal of the star[14]: (1) a nightly RV offset, (2) a Gaussian process regression and (3) diagnostics decorrelation with a moving average. For the inner transiting planet (K2-229 b), the three methods give consistent results (see Supplementary Fig. 3). Its mass determination is therefore robust in regard to stellar activity. The reflex motion of planet c is only significantly detected with method 3 and thus requires further investigations to be fully secured. The outer transiting planet (planet d) is not significantly detected in the RV data with any of the methods. We finally adopted the physical parameters of the K2-229 system, which are reported in Table 1, using model 2 for the correction of the activity-induced RVs.

The inner transiting planet, K2-229 b, has a mass of 2.59 ± 0.43 Earth masses ($M_\oplus$) and a radius of 1.165 ± 0.066 Earth radii ($R_\oplus$), hence a bulk density of 8.9 ± 2.1 g cm^{-3}. The planets c and d have masses less than 21.3 $M_\oplus$ and 25.1 $M_\oplus$ (95% credible interval), and radii of 2.12 ± 0.11 $R_\oplus$ and 2.65 ± 0.24 $R_\oplus$, respectively. Note that for the outer transiting planet, K2-229 d, we find two different orbital solutions: with an orbital period close to 31 d or longer than about 50 d. This bimodal distribution is due to the gap in the first half

Table 1 | List of the main physical parameters of the K2-229 planetary system

Parameter	Value and 68.3% credible interval		
	Host star		
Effective temperature $T_{\rm eff}$ (K)	$5{,}185 \pm 32$		
Surface gravity $\log g$	$4.56^{+0.03}_{-0.05}$		
Iron abundance (Fe/H) (dex)	-0.06 ± 0.02		
Mass $M_\star$ ($M_\odot$)	$0.837^{+0.019}_{-0.025}$		
Radius $R_\star$ ($R_\odot$)	$0.793^{+0.032}_{-0.020}$		
Age τ (stellar evolution tracks) (Gyr)	$5.4^{+5.2}_{-3.7}$		
Age τ (abundance ratio) (Gyr)	3.0 ± 0.9		
Distance to Earth D (pc)	104 ± 4		
Rotational velocity $v \sin i_\star$ (km s^{-1})	2.4 ± 0.5		
Rotation period $P_{\rm rot}$ (d)	18.1 ± 0.3		
Chromospheric activity index $\log R'_{\rm HK}$	-4.58 ± 0.04		
	Planet b	**Planet c**	**Planet d**
Period P (d)	$0.584249 \pm 1.4 \times 10^{-5}$	$8.32834 \pm 4.5 \times 10^{-4}$	31.0 ± 1.1
Eccentricity e	0 (assumed)	0 (assumed)	0.39 ± 0.29
Semi-major axis a (AU)	$0.012888 \pm 1.3 \times 10^{-4}$	$0.07577 \pm 7.6 \times 10^{-4}$	$0.1820 \pm 4.2 \times 10^{-3}$
Inclination i (°)	83.9 ± 2.8	87.94 ± 0.18	88.92 ± 0.24
Radius $R_{\rm p}$ ($R_\oplus$)	$1.164^{+0.066}_{-0.048}$	$2.12^{+0.11}_{-0.08}$	2.65 ± 0.24
Mass $M_{\rm p}$ ($M_\oplus$)	2.59 ± 0.43	<21.3[a]	<25.1[a]
Bulk density $\rho_{\rm p}$ (g cm^{-3})	8.9 ± 2.1	<12.8[a]	<9.5[a]
Equilibrium temperature[b] $T_{\rm eq}$ (K)	$1{,}960 \pm 40$	800 ± 20	522 ± 13
Day-side temperature[c] $T_{\rm d}$ (K)	$2{,}332 \pm 56$	962 ± 23	-

[a]95% credible upper limit.[b]Assuming a zero albedo.[c]Assuming a zero albedo and a tidally synchronized rotation.

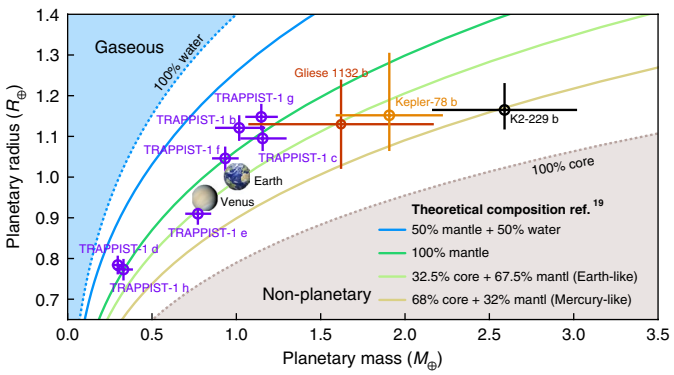

Fig. 2 | Mass–radius diagram of known Earth-sized planets. Only planets that have a mass measured with a precision better than 50% are shown here. The different lines represent possible theoretical compositions for terrestrial worlds[19]. Objects denser than 100% core are considered to be non-planetary, and those less dense than 100% water are considered to be gaseous. Credit: NASA exoplanet archive. Error bars are confidence intervals.

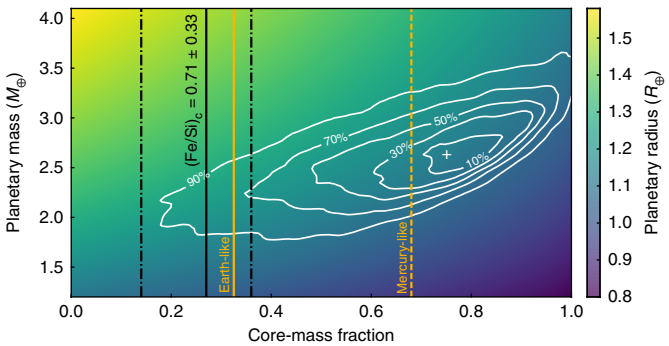

Fig. 3 | Theoretical radii of dry terrestrial worlds as a function of their total mass and core-mass fraction (assuming no water) for the planet K2-229 b. The + mark represents the mode of the posterior distribution. The white contours represent the 10%, 30%, 50%, 70% and 90% percentiles of the posterior distribution. The vertical solid and dot-dashed black lines represent the core-mass fraction and 1σ uncertainties, respectively, which correspond to $(Fe/Si)_c = 0.71 \pm 0.33$ as measured in the host star. The vertical solid and dashed orange lines indicate the Earth- and Mercury-like core-mass fractions, respectively.

of the K2 light curve (see Fig. 1). In the first case, another transit should have occurred during this gap, while in the second case, there is only one transit event during the entire photometric campaign. We excluded the long-period scenario for stability reasons, as this requires large eccentricity to explain the relatively short transit duration ($2.65^{+0.15}_{-0.20}$ h, see Supplementary Table 6), making planet d likely to cross the orbit of planet c.

In Fig. 2, we compare K2-229 b with other known Earth-sized planets[15–18], together with theoretical compositions of terrestrial planets (assuming different fractions of metallic core, silicate mantle and water layer)[19]. A comparison between K2-229 b and large rocky exoplanets as well as the rocky planets and major moons in the Solar System is also available in Supplementary Fig. 7. Given its high density of 8.9 ± 2.1 g cm^{-3}, we can constrain the water mass fraction to be less than a few percent at maximum and thus negligible in the planetary mass budget. Assuming K2-229 b is composed of only a metallic core (with a negligible fraction of silicon

(Si)) and a silicate mantle, its mass and radius are consistent with a core-mass fraction of 68^{+17}_{-25}% (ref. [19]). The derived core-mass fraction differs from the one computed (27^{+9}_{-13}%, see Fig. 3) assuming the planet was formed with the same Fe/Si corrected ($(Fe/Si)_c$) ratio (see Methods for a description of $(Fe/Si)_c$) as observed in the host star ($(Fe/Si)_c = 0.71 \pm 0.33$). Therefore, the composition of this planet is probably (with an 88% credible probability) different from the one expected based on the chemical composition of its host star. The reasons for this would be that the planet evolved since its formation, for instance by losing parts of its mantle[4,5], or it was formed with a substantially different $(Fe/Si)_c$ ratio than its host star[6]. With such a potentially large core-mass fraction, K2-229 b stands out as a larger analogue of Mercury in the Solar System, which has a core-mass fraction of 68% (refs [2,3]). Both planets might therefore share a common formation and evolution history.

Compared with Mercury, K2-229 b orbits much closer to its star, with an orbital period of about 14 h. Its day-side temperature can reach up to 2,330 K, assuming synchronous rotation. These conditions make K2-229 b potentially more sensitive than Mercury to mantle evaporation. At this temperature, the mantle in the day-side of the planet is expected to volatilize into a saturated atmosphere of silicate vapour[20]. Substantial evaporation of this atmosphere would result in planetary mass loss. Current thermal escape and stellar X-ray irradiation, however, are not expected to strip out this thin atmosphere substantially (see Methods). Other extremely hot rocky worlds have been reported with masses and radii consistent with an Earth-like composition[1], while a temperate, probably metal-rich, rocky planet has been recently detected: LHS 1140 b (ref. [21]). Therefore, stellar irradiation is not expected to contribute to the mass-loss rate (hence mantle evaporation) by more than a few percent of the total planetary mass.

Since K2-229 b is orbiting extremely close to an active K dwarf (at 0.012 AU), another hypothesis is that the thin layer of silicate vapour might escape from the planet through magnetic interaction with the host star[22,23]. Intense stellar wind and flares might also erode the planet's atmosphere[24]. However, these two mechanisms would be less efficient if the planet has its own magnetosphere, protecting the atmosphere from evaporation. More observations and modelling, which are outside the scope of this paper, are required to constrain this evolution scenario fully. The detection of a cometary-like tail[25] in the planet vicinity would be evidence for these mechanisms evaporating the volatilized mantle of rocky planets. Searching for a correlation between the core-mass fraction of rocky exoplanets and their magnetic environment[26] would provide insights into the importance of the magnetic field in this potential mechanism.

Another scenario to explain the composition of Mercury is a Theia-like giant impact[4]. If this scenario is responsible for Mercury-like exoplanets, there might be some correlation between the multiplicity and architecture of the systems with the presence of such planets. In that case, these planets would also be prime targets to search for relatively large exomoons. However, more giant-impact modelling is needed to understand what would be the initial conditions in terms of, for example, mass and velocity, for a Theia-like object to remove the mantle of rocky planets much more massive than Mercury such as K2-229 b.

Finally, if photophoresis is the mechanism that forms Mercury-like planets[6], the comparison of their host star's properties with those hosting Earth-like planets[1] will provide important constraints on the conditions required for this process. However, given the properties of the Mercury- and Earth-like planets (the orbital separation versus the core-mass fraction), there is no clear correlation between the formation conditions and the composition of the innermost planet. One possibility would be that the Earth-like planets are formed further out in the disk than those with a Mercury-like composition. Further theoretical work is needed to understand fully the formation and migration of these planets under the photophoresis scenario.

Note that after we submitted this paper, the planet K2-106 b, which was initially reported with an Earth-like composition[27], has been found to be much more rich in iron[28]. No clear comparison between the composition of K2-106 b and the one of its host star has been performed so far. Still, it shows that the existence of such Mercury-like planets is more common than previously thought. This is opening a new approach to understand the particular formation and evolution of these planets.

The planet K2-229 b appears to have abundances that are different from the ones of the central star. This is the first time such a situation has been observed in an extrasolar system[29]. Its composition is similar to that of Mercury. However, both planets do not share the same environmental conditions, the former being substantially hotter and closer to its star. Therefore, K2-229 b is an excellent laboratory to test the conditions to form Mercury analogues. The exploration of this new population of exoplanets can greatly complement Solar System in situ missions such as MESSENGER (MErcury Surface, Space ENvironment, GEochemistry and Ranging) and BepiColombo[8], and will help to constrain the formation and evolution mechanisms of Mercury-like planets in various environments. It can then be used to refine the formation models of the Solar System terrestrial planets. The increased precision in mass and radius measurements brought by upcoming dedicated missions such as PLATO (PLAnetary Transits and Oscillations of stars)[30] will bring an important advancement for this purpose.

Methods

K2 light-curve reduction and transit detection. The search for candidates followed a process incorporating automated searches and human vetting. The POLAR-detrended[9] K2 light curves are first flattened using a moving third-degree polynomial filter, iteratively fit 20 times to a 3.5 d region while ignoring outliers from the previous fit. The polynomial is not allowed to fit across gaps in the data greater than 1 d. After flattening, light curves are run through a modified box-fitting least-squares search[31], where outliers across the campaign are ignored from all light curves. We rank light curves on their box-fitting least-squares signal strength, then individually vet every light curve through human eyeballing. Candidates are passed on for follow-up if they pass a number of tests: there must be no visible nearby companions, no visible centroid motion during transit and no significant depth difference between odd and even transits. We further rank successful candidates using their transit shape, as measured by the θ_2 statistic[32], which uses self-organizing maps to distinguish between planetary and false-positive transit shapes.

RV observations and reduction. The RV observations were carried out with the HARPS spectrograph, mounted on the European Southern Observatory (ESO) 3.6 m Telescope in La Silla Observatory in Chile. HARPS is a fibre-fed echelle spectrograph with a resolving power $R \approx 110{,}000$, optimized for precise RV observations[33]. The spectroscopic data were obtained as part of our ESO–K2 large programme (ESO programme ID: 198.C-0169). We used an exposure time of 1,800 s for individual observations, which led to signal-to-noise ratios at the level of 60 per CCD (charge-coupled device) pixel at 550 nm. Spectra were reduced with the online pipeline. One spectrum failed the automatic quality checks of the pipeline due to an incorrect colour-flux correction. The RVs were derived following the standard procedure used for more than two decades[34], consisting of cross-correlating the observed spectra with a numerical mask corresponding to a G2V star. From the result of the cross-correlation function, we derived the RV, the BIS, the FWHM and their associated uncertainties[35,36]. RVs have a median precision of 1.7 m s^{-1}. From the spectra, we also measured indices of chromospheric emission, S_{MW} (Mount Wilson Observatory S index), $I_{H\alpha}$, I_{NaD} and I_{HeID3}, in the activity-sensitive calcium II H and K, Hα, sodium I D and helium I D3 lines, respectively[37]. All these data are available in Supplementary Tables 3 and 4.

From the FWHM values, we estimated the sky-projected stellar rotational velocity to be $v \sin i_\star = 2.4 \pm 0.5$ km s^{-1}, where v is the rotational velocity and $i_\star$ is the stellar inclination. Using the S_{MW}, which evaluates the level of chromospheric emission in the calcium II H and K lines, we computed the value of the chromospheric activity index $\log R_{HK}$ (ref. [38]) to be -4.58 ± 0.04. The S_{MW} data clearly show a long-term slope with a value of -0.14 ± 0.02 yr^{-1}. This drift is also observed in the FWHM and $I_{H\alpha}$ (see Supplementary Fig. 1), and might reveal a rapidly evolving or large-amplitude magnetic cycle, the star being less active at the end of the campaign than at the start.

Spectroscopic analysis and chemical composition of the star. The stellar parameters (T_{eff}, [Fe/H], $\log g$ and v_{mic}) were derived from the Doppler-corrected co-added HARPS spectra with the same methods as stars in the SWEET-Cat

catalogue[11]. This method uses standard local thermodynamical equilibrium analysis with the 2014 version of the code MOOG (ref. [39]). A grid of Kurucz ATLAS9 atmospheres[40] was used as input along with the equivalent widths measured automatically with version 2.0 of the ARES program[41]. The log$g$ value, known to be systematically biased, was corrected using a calibration based on asteroseismic targets[42]. The derived values are $T_{\rm eff}=5{,}120\pm39$ K, $\log g=4.51\pm0.12$ cm s^{-2}, [Fe/H] $=-0.06\pm0.02$ dex and $v_{\rm mic}=0.74\pm0.08$ km s^{-1}. These values were then used as priors in the Bayesian joint analysis described below. The adopted values, reported in Table 1, are the posteriors of this joint analysis and are thus consistent with the SED and the stellar density as constrained by the transit.

Elemental abundances were determined with the same approach as the analysis of the HARPS Guaranteed Time Observations sample[43]. Lithium abundance was derived with a spectral synthesis method also by using the code MOOG and ATLAS atmospheres[44]. Using the yttrium/magnesium abundance ratio [Y/Mg], we estimated the age[45] of the star to be 3.0 ± 0.9 Gyr.

Lucky-imaging observations. We obtained a high-spatial-resolution image of the target with the AstraLux camera[46] installed at the 2.2 m telescope of the Calar Alto Observatory. By using the lucky-imaging technique to avoid atmospheric distortions, we obtained 90,000 images in the Sloan Digital Sky Survey i′ band of 30 ms exposure time, well below the coherence time. Note that the Sloan filters use the AB magnitude system. We used the observatory pipeline to perform the basic reduction of the images and the subsequent selection of the 10% best-quality frames, with the highest Strehl ratios (total integration time of 270 s). These images are then aligned and combined to obtain the final high-spatial-resolution image, shown in Supplementary Fig. 2 together with the $80\times80''$ image of the Digitized Sky Survey and the K2 photometric mask. No other companion closer than 12″ and within the sensitivity limits is detected. We estimated the sensitivity curve[47] of this high-spatial-resolution image, shown in Supplementary Fig. 2.

Due to the decentring of the K2 mask compared with the AstraLux image, we also checked for companions in the Digitized Sky Survey image and found only a faint target (magnitude difference of 8.1 in the R band) outside the K2 best aperture. The contamination from this source is thus negligible. Consequently, we can conclude that the extracted K2 light curve is not contaminated within our sensitivity limits. We computed the background source confidence[47], which illustrates the confidence to which we can affirm that our planet signal is not affected by relevant chance-aligned sources up to a certain separation. In this case, we obtained background source confidence values of 98.32%, 99.44% and 99.67%, for planets b, c and d, respectively. Therefore, we can conclude that the chances of having missed a relevant contaminant in this high-spatial-resolution image are very small for any of the detected planets.

Bayesian analysis of photometry, RV and SED. We jointly analysed the K2 photometry, HARPS RVs and the SED in a Bayesian framework. We used the K2SFF (K2 Self Flat-Fielding) reduction[48] of the K2 light curve with the optimal aperture mask that we corrected for spot and faculae modulation as well as residuals of instrumental systematics, using a Gaussian process regression with a Matérn 3/2 kernel[49], trained on out-of-transit photometry. For the SED, we used the optical magnitudes from the American Association of Variable Star Observers Photometric All-Sky Survey[50], and near-infrared magnitudes from the Two-Micron All-Sky Survey and Wide-field Infrared Survey Explorer[51]. These magnitudes are reported in Supplementary Table 1. The light curve was modelled with the JKTEBOP (JKT Eclipsing Binary Orbit Program)[52] with an oversampling factor of 30 to account for the long exposure time of Kepler[53]. The SED was modelled with the BT-Settl stellar atmosphere models[54]. For the RV, we used three different models, described below, to account for the Keplerian orbit of the three planets and the stellar variability. We did not oversample the RV model to account for the relatively long exposure time (3.5% of the period of the inner planet), as this effect is expected to underestimate the planetary mass by less than 0.2%, which is negligible.

To account for the asterodensity profiling[55], we modelled the central star with the Dartmouth stellar evolution tracks[56]. Note that we also used the PARSEC (PAdova and TRieste Stellar Evolution Code) evolution tracks[57] with no significant change in the result. Linear and quadratic limb-darkening coefficients were taken from a commonly adopted theoretical table[58] and are changed in the analysis as a function of the stellar parameters.

The analysis was performed using PASTIS[13], which runs a Markov chain Monte Carlo algorithm. The exhaustive list of parameters and their respective priors is available in Supplementary Tables 5–7 and displayed in Supplementary Figs. 4–6. For each of the activity-correction methods, we run 20 Markov chain Monte Carlo simulations of 3×10^5 iterations, initialized at random points drawn from the joint prior distribution. The chains were tested for convergence using a Kolmogorov–Smirnov test[59]. The burn-in of each chain was removed before merging them to derive the posterior distribution, from which we computed the median and 68.3% credible interval for each parameter. When necessary, we kept only the samples of the posterior distributions for which the stellar age, as provided by the evolution tracks, is compatible with the age of the Universe. Similar analyses have previously been performed to characterize several transiting companions, from brown dwarfs to low-mass planets[60–62].

Activity-correction method 1: a nightly RV offset. A straightforward method to correct for stellar activity when characterizing ultrashort-period planets is to account for a nightly RV offset[63]. This requires that several observations are taken each night, which is the case here. This method assumes that the activity of the star does not evolve substantially within the night, but filters out any signal with a period longer than about 1 d. Therefore, this model can be used to characterize only the inner transiting planet, K2-229 b.

The function $\mathbf{f}$ to describe the RV data is the following:

$$\mathbf{f}=\gamma+\mathbf{k}_{j=1}+\mathbf{\Delta\gamma}_l \tag{1}$$

$$\mathbf{k}_j=K_j[\cos(\mathbf{v}_j+\omega_j)+e_j\cos(\omega_j)] \tag{2}$$

where γ is the systemic RV, $\mathbf{k}_j$ is the Keplerian orbit model of the jth planet and $\mathbf{\Delta\gamma}_l$ is the offset of the lth night. The Keplerian orbit of the jth planet is described by the RV semi-amplitude, K_j, the true anomaly, $\boldsymbol{\nu}_j$, the eccentricity, e_j, and the argument of periastron, ω_j.

The target K2-229 was observed over 51 different nights with at least two and up to four observations. For the sake of simplicity, we here fixed the ephemeris of the inner planet to the best values (see Supplementary Table 5). We find no significant eccentricity, with $e_{j=1}=0.16\pm0.11$, as expected given the ultrashort period of the planet. Assuming a circular orbit, we find $K_{j=1}=2.82\pm0.40$ m s^{-1}, which translates into a mass for planet b of $M_{\rm b}=3.28\pm0.47\,M_\oplus$. Note that the RV activity signal varies up to 1.1 m s^{-1} over the ~5 h observations each night. This mass determination might thus be slightly biased depending on how the activity signal phases with the planet orbit at the time of the observations.

Activity-correction method 2: Gaussian process regression. Recently, Gaussian processes have been shown to be a robust statistical method to model stellar activity in RV data[14,64]. For that, we computed the likelihood $\mathcal{L}$ accounting for the covariance matrix[49].

$$\ln\mathcal{L}=-\frac{1}{2}\mathbf{r}^{\rm T}K^{-1}\mathbf{r}-\frac{1}{2}\ln|K|-\frac{n}{2}\ln(2\pi) \tag{3}$$

$$\mathbf{r}=\mathbf{y}-\left[\gamma+\sum_{j=1}^{3}\mathbf{k}_j\right] \tag{4}$$

$$K=A^2\exp\left[-\frac{1}{2}\left(\frac{\Delta t}{\lambda_1}\right)^2-\frac{2}{(\lambda_2)^2}\sin^2\left(\frac{\pi\Delta t}{P_{\rm rot}}\right)\right]+I\sqrt{\boldsymbol{\sigma}^2+\sigma_{\rm jit}^2} \tag{5}$$

where n is the number of observations, $\mathbf{r}$ is the residual between the three-Keplerian-orbit model and the data $\mathbf{y}$, and K is the covariance matrix. We used here a quasi-periodic kernel[49] (equation (5)) with the hyperparameters: amplitude, A, rotation period, $P_{\rm rot}$, coherent timescale of the active region, λ_1, and relative weight between the periodic and decay terms, λ_2. The matrix Δt is the differential time such that $\Delta t_{ij}=t_i-t_j$. Finally, I is the identity matrix, $\boldsymbol{\sigma}$ is the Gaussian uncertainty vector associated with the data and $\sigma_{\rm jit}$ is an extra source of uncorrelated (jitter) noise.

We first trained the Gaussian process hyperparameters on the K2 light curve. However, because of the 15 d gap in the first part of the campaign, the rotation period was constrained to $P_{\rm rot}=18.1\pm1.1$ d. We also trained the Gaussian process hyperparameters on the spectroscopic diagnoses. We find rotation periods of 18.1 ± 0.3 d, 19.2 ± 0.4 d, 18.1 ± 0.2 d, 18.4 ± 0.3 d, 17.1 ± 0.4 d and 17.9 ± 1.0 d by training on the $S_{\rm MW}$, FWHM, BIS, $I_{\rm H\alpha}$, $I_{\rm NaD}$ and $I_{\rm HeiD3}$, respectively. All these estimates of the rotation period are fully consistent, and we finally adopted the one based on the $S_{\rm MW}$, hence $P_{\rm rot}=18.1\pm0.3$ d.

We analysed the HARPS RVs of K2-229 with a three-Keplerian-orbit model and a Gaussian process as described above. We used uninformative priors for the hyperparameters, except for $P_{\rm rot}$, for which we use a normal distribution of 18.1 ± 0.3 d.

We first allowed the eccentricity of the three planets to vary. We find non-significant eccentricities with $e_{j=1}=0.08^{+0.08}_{0.06}$, $e_{j=2}=0.30^{+0.36}_{0.13}$ and $e_{j=3}=0.32\pm0.31$ for planets b, c and d, respectively. We thus assumed circular orbits for the two inner planets, which have orbital periods of less than 10 d and are probably circularized. We find RV amplitudes of $K_{j=1}=2.23\pm0.35$ m s^{-1}, $K_{j=2}=3.2\pm2.4$ m s^{-1} and $K_{j=3}=2.4^{+2.8}_{-1.6}$ m s^{-1} for planets b, c and d, respectively. This corresponds to a mass for planet b of $M_{\rm b}=2.59\pm0.43\,M_\oplus$. Planets c and d have only upper limits on their masses, of 21.3 $M_\oplus$ and 25.1 $M_\oplus$ with a 95% credible probability, respectively. The RV residuals from the best model have a scatter of 1.6 m s^{-1}, which is fully compatible with the median photon noise on this star (1.7 m s^{-1}). We therefore adopted this solution for the system.

Activity-correction method 3: decorrelation of the spectroscopic diagnoses and moving average. The final approach to correct for stellar activity in RV data uses

the spectroscopic diagnoses (for example, FWHM, BIS, S_{MW}, $I_{H\alpha}$)[65]. This technique then assumes a linear correlation between the RVs and each of the diagnoses. The coefficients of the linear correlation are fitted simultaneously with the Keplerian orbit models. The model f for each observing time t_i described below also accounts for a moving average with an exponential decay in time. This method was shown to be efficient to correct for activity-induced RV variation in the recent RV challenge[14].

$$\begin{aligned} f(t_i) &= \gamma + at_i + bt_i^2 + \sum_{j=1}^{3} k_j(t_i) \\ &+ c_{n=0}(\mathrm{BIS}(t_i) - \mathrm{BIS}_0) + c_{n=1}(\mathrm{FWHM}(t_i) - \mathrm{FWHM}_0) \\ &+ c_{n=2}(S_{\mathrm{MW}}(t_i) - S_{\mathrm{MW},0}) + c_{n=3}(I_{\mathrm{H}\alpha}(t_i) - I_{\mathrm{H}\alpha,0}) \\ &+ \phi\left[f(t_{i-1}) - \sum_{j=1}^{3} k_j(t_{i-1})\right]\exp\left(\frac{t_{i-1}-t_i}{\tau}\right) \end{aligned} \quad (6)$$

where a and b are coefficients for a possible linear and quadratic (respectively) long-term drift, c_n are the coefficients for the linear correlation with the spectroscopic diagnoses. The parameters BIS_0, FWHM_0, $S_{\mathrm{MW},0}$ and $I_{\mathrm{H}\alpha,0}$ are the zero point of the corresponding diagnoses. The moving average has two parameters: its amplitude, ϕ, and its time decay,τ.

The spectroscopic diagnoses I_{NaD} and I_{HeID3} were not used in this model, because the activity signal is only barely detected in these data. Note that we tested the influence of each diagnosis, and the best solution is found when the moving average is used together with the BIS, FWHM and S_{MW} indices. Including $I_{\mathrm{H}\alpha}$ or not in the model does not significantly change the solution, as this diagnosis is redundant with S_{MW} at our level of precision. This implies that $c_{n=2}$ and $c_{n=3}$ are fully degenerated. Nevertheless, we included $I_{\mathrm{H}\alpha}$ in the analysis as this has no significant effect on the result.

As for the previous methods, we first let the eccentricity of the three planets vary in the analysis, and find $e_{j=1} = 0.20 \pm 0.11$, $e_{j=2} = 0.24 \pm 0.12$ and $e_{j=3} = 0.49 \pm 0.39$ for planets b, c and d, respectively. Since the orbits of the two inner planets, which are expected to be circularized, have no significant eccentricity, we then assumed them to be circular. We find RV semi-amplitudes of $K_{j=1} = 2.11 \pm 0.73\,\mathrm{m\,s^{-1}}$, $K_{j=2} = 3.33 \pm 0.85\,\mathrm{m\,s^{-1}}$ and $K_{j=3} = 1.1^{+1.4}_{-0.7}\,\mathrm{m\,s^{-1}}$ for planets b, c and d, respectively. This translates into masses for planets b and c of $M_b = 2.45 \pm 0.84\,M_\oplus$ and $M_c = 9.3 \pm 2.4\,M_\oplus$, respectively. For planet d, we measured only an upper limit on the mass at $11.5\,M_\oplus$ with a 95% credible probability. These values are fully compatible with the ones derived with the other methods. This method gives an uncertainty for planet b twice as large as the two other methods, but allows us to measure the mass of planet c tentatively. The RV residuals of the best model have a scatter at the level of $5.5\,\mathrm{m\,s^{-1}}$, which is significantly higher than the median photon noise ($1.7\,\mathrm{m\,s^{-1}}$). Thus, this model does not fully correct the activity-induced RVs for this star.

Likelihood of planetary signals. We have significantly detected the reflex motion of the host star caused by the orbit of planet b, with three different methods to correct for stellar activity. The spectroscopic diagnoses, which might reveal false-positive scenarios[35], show no significant variation at the orbital period of planet b (with false-alarm probabilities larger than 50%) in the Gaussian process-corrected data (see Supplementary Fig. 1). Moreover, if the RV variations caused by planet b were correlated with the BIS or FWHM, method 3 would have probably absorbed its Keplerian signal. Moreover, the AstraLux high-resolution imaging revealed no contaminating stars within the sensitivity limits. We therefore conclude that planet b is a bona fide transiting planet.

The Keplerian signal of planet c is detected only with method 3. Once again, if this RV signal was correlated with spectroscopic diagnoses, it would have been unlikely to be detected with this method. Using the planet-multiplicity likelihood boost[66], we consider planet c is also a bona fide transiting planet.

With only a unique and partial transit and no detection in the RV data, planet d is not fully secured. More photometric observations are needed to confirm the presence of this third planet in the system. If this monotransit event is real, given that two planets are already transiting in this system and no background star is detected in the photometric mask within the AstraLux sensitivity, planet d would probably be a bona fide transiting planet.

Planetary composition. To probe the composition of K2-229 b, we used a model of planetary interior models based on the physical properties of Earth and terrestrial planets[19]. All planets considered in this model are fully differentiated into three main layers: a metallic core, a silicate mantle and a water envelope. In the case of K2-229 b, given its high density, we can constrain from our simulations that the water mass fraction is less than about 10% if in liquid phase, with almost no mantle. Assuming water in supercritical or gaseous phase decreases the water mass fraction to a few percent only at maximum. Thus, we consider only solid terrestrial structures in this work. In our model, the core is composed of Fe and the iron–sulfur alloy FeS in proportions 87% to 13%, as in the case of Earth[67]. We note that other volatiles (for example, silicon, oxygen and carbon) are commonly used to model the Earth's core[68] with abundances up to a few percent. For the sake of simplicity, here we consider only sulfur in our model; it is assumed as a proxy of all volatiles.

The silicate mantle might be divided into two sublayers: a lower mantle composed of bridgmanite and ferropericlase, and an upper mantle composed of olivine and enstatite, due to a phase transition induced by the pressure gradient inside the planet. The size and thus mass of the core and mantle fix the distribution of materials inside a planet, that is, its composition. From this, a planet's composition is entirely described by a single parameter, namely its core-mass fraction. In our simulations, we assumed the surface conditions of K2-229 b to be 1 bar pressure, with a surface temperature equal to the derived equilibrium temperature. At this temperature, the silicate mantle would be liquid on the surface of the planet; however, we do not consider here this phase transition, as the density of liquid silicates differs from that of the solid phase by only a few percent[20,69]. The model computes a planetary radius from a given planetary mass and an assumed composition (or core-mass fraction). We thus explored the full 0–100% range for the core-mass fraction, and a limited range for the planetary mass (see Fig. 3), to constrain the composition of K2-229 b from its measured fundamental parameters.

For terrestrial planets, the core-mass fraction is directly linked to the bulk Fe/Si and magnesium Mg/Si ratios[19]. As these ratios cannot be measured, we assumed them to be consistent with the stellar values[7,29]. Using the stellar abundances from Supplementary Table 2, which are relative to that of the Sun[70], we find Fe/Si $= 0.70 \pm 0.33$ and Mg/Si $= 0.89 \pm 0.37$ for K2-229. For terrestrial planets, these values can be corrected to include elements that are not considered in the model (aluminium, calcium and nickel) but represent a non-negligible part of the planets' mass[67,71]. Taking into account these elements, we computed corrected ratios $(\mathrm{Fe/Si})_c = 0.71 \pm 0.33$ and $(\mathrm{Mg/Si})_c = 0.98 \pm 0.40$. The core-mass fraction of a planet is essentially governed by the Fe/Si ratio, as in our model, Fe is mostly found in the core, whereas Mg and Si are found only in the mantle. As shown in Fig. 3, $(\mathrm{Fe/Si})_c = 0.71 \pm 0.33$ corresponds to a core-mass fraction of 27^{+9}_{-13}%. As they are measured relative to the Sun, the derived Fe/Si and Mg/Si absolute ratios of the star can vary substantially depending on the various solar abundances available in the literature[72,73]. Using different values for the solar abundances, we find that the difference between the expected core-mass fraction, derived from the stellar $(\mathrm{Fe/Si})_c$, and the one derived from the fundamental parameters of K2-229 b remains: $(\mathrm{Fe/Si})_c = 0.82 \pm 0.25$ (hence a core-mass fraction of 26^{+6}_{-8}%)[73] or $(\mathrm{Fe/Si})_c = 0.74 \pm 0.26$ (hence a core-mass fraction of 28^{+7}_{-9}%)[72]. Therefore, the expected value of the core-mass fraction is not sensitive to the values used for the solar abundances.

The validity of these results assumes no inclusion of Si in the planet's core. If Si is actually present in the core in substantial amounts, it would change the planetary Fe/Si towards a more stellar value, hence impacting our conclusion. However, in the case of the Earth's core, the fraction of Si is constrained at the level of a few percent at maximum[68].

Mantle evaporation. The volatilization of the atmosphere might be achieved by stellar irradiation. Considering that the escape is energy limited, the mass-loss rate $\dot{m}$ is obtained by equalizing the gravitational potential with the incident energy flux:

$$\dot{m} = \epsilon \frac{L_X R_p^3}{G M_p (2a)^2} \quad (7)$$

where L_X is the X-ray luminosity, R_p is the planetary radius, M_p is the planetary mass, a is the semi-major axis, G is the gravitational constant and ϵ is an efficiency factor estimated[74] as $\epsilon \approx 0.12$. We estimated the X-ray flux[75] as $L_X \approx 1.4\,(v \sin i_\star)^{1.9} = 7.6 \times 10^{27}\,\mathrm{erg\,s^{-1}}$. The mass-loss rate through irradiation is then $\dot{m} = 1.3 \times 10^{-5}\,M_\oplus\,\mathrm{Myr^{-1}}$. Note that this is slightly underestimated as the irradiation occurs in the exosphere and not at the planetary surface. This mass-loss rate was also substantially higher in the early stage of the system, when the star was younger and thus more active. Depending on the system's age, this mechanism might have eroded the atmosphere at the level of only a few percent of the total planetary mass.

The volatilization of the atmosphere might also be achieved by Jeans (or thermal) escape. In that case, the particle-loss rate is given by the Jeans formula

$$F_J = \frac{N_{ex} v_0}{2\sqrt{\pi}} (1 + \lambda_{esc}) e^{-\lambda_{esc}} \quad (8)$$

where N_{ex} is the particle density at the exobase, $v_0 = \sqrt{\frac{2 k_B T}{m}}$ is the mean thermal velocity of a particle of mass m, T is the temperature, k_B is the Boltzmann constant and λ_{esc} is the adimensional escape parameter, defined as

$$\lambda_{esc} = \frac{G M_p m}{k_B T (R_p + H)} \quad (9)$$

where H is the exobase height.

To compute F_J, we assumed that the gaseous enstatite is completely photodissociated in an ideal gas of mean molecular weight $M_{mol} \approx 11\,\mathrm{g\,mol^{-1}}$.

Under these conditions, we get a mass-loss rate of $5.2\times10^{-33}\,M_{\oplus}\,\mathrm{Myr}^{-1}$. Even at the extreme yet possible temperature of 10^4 K at the exobase, the mass-loss rate reaches only $2.8\times10^{-14}\,M_{\oplus}\,\mathrm{Myr}^{-1}$, which means that this process is not sufficient to explain the high density of K2-229 b.

Data availability. The data that support the plots within this paper and other findings of this study are available from the corresponding author upon reasonable request.

Received: 23 June 2017; Accepted: 13 February 2018;
Published online: 26 March 2018

References

1. Dressing, C. D. et al. The mass of Kepler-93b and the composition of terrestrial planets. *Astrophys. J.* **800**, 135 (2015).
2. Stacey, F. D. High pressure equations of state and planetary interiors. *Rep. Prog. Phys.* **68**, 341 (2005).
3. Smith, D. E. et al. Gravity field and internal structure of Mercury from MESSENGER. *Science* **336**, 214–217 (2012).
4. Benz, W., Anic, A., Horner, J. & Whitby, J. A. in *Mercury* (eds Balogh, A. et al.) 7–20 (Vol. 26, Space Sciences Series of ISSI, Springer, New York, USA, 2008).
5. Cameron, A. The partial volatilization of Mercury. *Icarus* **64**, 285–294 (1985).
6. Wurm, G., Trieloff, M. & Rauer, H. Photophoretic separation of metals and silicates: the formation of Mercury-like planets and metal depletion in chondrites. *Astrophys. J.* **769**, 78 (2013).
7. Thiabaud, A., Marboeuf, U., Alibert, Y., Leya, I. & Mezger, K. Elemental ratios in stars vs planets. *Astron. Astrophys.* **580**, A30 (2015).
8. Benkhoff, J. et al. BepiColombo—comprehensive exploration of Mercury: mission overview and science goals. *Planet. Space. Sci.* **58**, 2–20 (2010).
9. Barros, S., Demangeon, O. & Deleuil, M. New planetary and eclipsing binary candidates from campaigns 1–6 of the K2 mission. *Astron. Astrophys.* **594**, A100 (2016).
10. Huber, D. et al. The K2 Ecliptic Plane Input Catalog (EPIC) and stellar classifications of 138,600 targets in campaigns 1–8. *Astrophys. J. Suppl. Ser.* **224**, 2 (2016).
11. Santos, N. et al. SWEET-Cat: a catalogue of parameters for stars with exoplanets—I. new atmospheric parameters and masses for 48 stars with planets. *Astron. Astrophys.* **556**, A150 (2013).
12. Dumusque, X., Boisse, I. & Santos, N. SOAP 2.0: a tool to estimate the photometric and radial velocity variations induced by stellar spots and plages. *Astrophys. J.* **796**, 132 (2014).
13. Daz, R. F. et al. PASTIS: Bayesian extrasolar planet validation—I. general framework, models, and performance. *Mon. Not. R. Astron. Soc.* **441**, 983–1004 (2014).
14. Dumusque, X. et al. Radial-velocity fitting challenge—II. first results of the analysis of the data set. *Astron. Astrophys.* **598**, A133 (2017).
15. Pepe, F. et al. An Earth-sized planet with an Earth-like density. *Nature* **503**, 377–380 (2013).
16. Berta-Thompson, Z. K. et al. A rocky planet transiting a nearby low-mass star. *Nature* **527**, 204–207 (2015).
17. Gillon, M. et al. Seven temperate terrestrial planets around the nearby ultracool dwarf star TRAPPIST-1. *Nature* **542**, 456–460 (2017).
18. Grimm, S. L. et al. The nature of the TRAPPIST-1 exoplanets. Preprint at https://arxiv.org/abs/1802.01377 (2018).
19. Brugger, B., Mousis, O., Deleuil, M. & Deschamps, F. Constraints on super-Earth interiors from stellar abundances. *Astrophys. J.* **850**, 93 (2017).
20. Léger, A. et al. The extreme physical properties of the CoRoT-7b super-Earth. *Icarus* **213**, 1–11 (2011).
21. Dittmann, J. A. et al. A temperate rocky super-Earth transiting a nearby cool star. *Nature* **544**, 333–336 (2017).
22. Lanza, A. Star-planet magnetic interaction and evaporation of planetary atmospheres. *Astron. Astrophys.* **557**, A31 (2013).
23. Strugarek, A. Assessing magnetic torques and energy fluxes in close-in star–planet systems. *Astrophys. J.* **833**, 140 (2016).
24. Garraffo, C., Drake, J. J., Cohen, O., Alvarado-Gomez, J. D. & Moschou, S. P. The threatening environment of the TRAPPIST-1 planets. Preprint at https://arxiv.org/abs/1706.04617 (2017).
25. Mura, A. et al. Comet-like tail-formation of exospheres of hot rocky exoplanets: possible implications for CoRoT-7b. *Icarus* **211**, 1–9 (2011).
26. Moutou, C., Donati, J.-F., Lin, D., Laine, R. & Hatzes, A. The magnetic properties of the star Kepler-78. *Mon. Not. R. Astron. Soc.* **459**, 1993–2007 (2016).
27. Sinukoff, E. et al. K2-66b and K2-106b: two extremely hot sub-Neptune-size planets with high densities. *Astron. J.* **153**, 271 (2017).
28. Guenther, E. et al. K2-106, a system containing a metal-rich planet and a planet of lower density. Preprint at https://arxiv.org/abs/1705.04163 (2017).
29. Dorn, C. et al. A generalized Bayesian inference method for constraining the interiors of super Earths and sub-Neptunes. *Astron. Astrophys.* **597**, A37 (2017).
30. Rauer, H. et al. The PLATO 2.0 mission. *Exp. Astron.* **38**, 249–330 (2014).
31. Kovács, G., Zucker, S. & Mazeh, T. A box-fitting algorithm in the search for periodic transits. *Astron. Astrophys.* **391**, 369–377 (2002).
32. Armstrong, D. J., Pollacco, D. & Santerne, A. Transit shapes and self-organizing maps as a tool for ranking planetary candidates: application to Kepler and K2. *Mon. Not. R. Astron. Soc.* **465**, 2634–2642 (2017).
33. Mayor, M. et al. Setting new standards with HARPS. *The Messenger* **114**, 20–24 (2003).
34. Baranne, A. et al. ELODIE: a spectrograph for accurate radial velocity measurements. *Astron. Astrophys. Suppl. Ser.* **119**, 373–390 (1996).
35. Santerne, A. et al. PASTIS: Bayesian extrasolar planet validation—II. constraining exoplanet blend scenarios using spectroscopic diagnoses. *Mon. Not. R. Astron. Soc.* **451**, 2337–2351 (2015).
36. Bouchy, F., Pepe, F. & Queloz, D. Fundamental photon noise limit to radial velocity measurements. *Astron. Astrophys.* **374**, 733–739 (2001).
37. Gomes da Silva, J. et al. Long-term magnetic activity of a sample of M-dwarf stars from the HARPS program. I. Comparison of activity indices. *Astron. Astrophys.* **534**, 30 (2011).
38. Noyes, R., Hartmann, L., Baliunas, S., Duncan, D. & Vaughan, A. Rotation, convection, and magnetic activity in lower main-sequence stars. *Astrophys. J.* **279**, 763–777 (1984).
39. Sneden, C. Carbon and nitrogen abundances in metal-poor stars. *Astrophys. J.* **189**, 493–507 (1974).
40. Kurucz, R. *ATLAS9 Stellar Atmosphere Programs and 2 km/s Grid* CD-ROM no. 13. (Smithsonian Astrophysical Observatory, 1993).
41. Sousa, S., Santos, N., Adibekyan, V., Delgado-Mena, E. & Israelian, G. ARES v2: new features and improved performance. *Astron. Astrophys.* **577**, A67 (2015).
42. Mortier, A., Sousa, S., Adibekyan, V. Z., Brandão, I. & Santos, N. Correcting the spectroscopic surface gravity using transits and asteroseismology—no significant effect on temperatures or metallicities with ARES and MOOG in local thermodynamic equilibrium. *Astron. Astrophys.* **572**, A95 (2014).
43. Adibekyan, V. Z. et al. Chemical abundances of 1111 FGK stars from the HARPS GTO planet search program—Galactic stellar populations and planets. *Astron. Astrophys.* **545**, A32 (2012).
44. Delgado Mena, E. et al. Li depletion in solar analogues with exoplanets—extending the sample. *Astron. Astrophys.* **562**, A92 (2014).
45. Maia, M. T. et al. The solar twin planet search—III. the [Y/Mg] clock: estimating stellar ages of solar-type stars. *Astron. Astrophys.* **590**, A32 (2016).
46. Hormuth, F., Brandner, W., Hippler, S. & Henning, T. AstraLux—the Calar Alto 2.2-m telescope Lucky Imaging Camera. *J. Phys. Conf. Ser.* **131**, 012051 (2008).
47. Lillo-Box, J., Barrado, D. & Bouy, H. High-resolution imaging of Kepler planet host candidates—a comprehensive comparison of different techniques. *Astron. Astrophys.* **566**, A103 (2014).
48. Vanderburg, A. & Johnson, J. A. A technique for extracting highly precise photometry for the two-wheeled Kepler mission. *Publ. Astron. Soc. Pac.* **126**, 948 (2014).
49. Rasmussen, C. E. & Williams, C. K. *Gaussian Processes for Machine Learning* Vol. 1 (MIT Press, Cambridge, MA, USA, 2006).
50. Henden, A. & Munari, U. The APASS all-sky, multi-epoch BVgri photometric survey. *Contrib. Astron. Obs. S.* **43**, 518–522 (2014).
51. Cutri, R. et al. *AllWISE Data Release (Cutri+ 2013)* (accessed 17 September 2017); http://vizier.u-strasbg.fr/viz-bin/VizieR?-source=%20ALLWISE
52. Southworth, J. Homogeneous studies of transiting extrasolar planets—I. light-curve analyses. *Mon. Not. R. Astron. Soc.* **386**, 1644–1666 (2008).
53. Kipping, D. M. Binning is sinning: morphological light-curve distortions due to finite integration time. *Mon. Not. R. Astron. Soc.* **408**, 1758–1769 (2010).
54. Allard, F., Homeier, D. & Freytag, B. Models of very-low-mass stars, brown dwarfs and exoplanets. *Phil. Trans. R. Soc. A* **370**, 2765–2777 (2012).
55. Kipping, D. M. Characterizing distant worlds with asterodensity profiling. *Mon. Not. R. Astron. Soc.* **440**, 2164–2184 (2014).
56. Dotter, A. et al. The Dartmouth Stellar Evolution Database. *Astrophys. J. Suppl. Ser.* **178**, 89 (2008).
57. Bressan, A. et al. PARSEC: stellar tracks and isochrones with the PAdova and TRieste Stellar Evolution Code. *Mon. Not. R. Astron. Soc.* **427**, 127–145 (2012).
58. Claret, A. & Bloemen, S. Gravity and limb-darkening coefficients for the Kepler, CoRoT, Spitzer, uvby, UBVRIJHK, and Sloan photometric systems. *Astron. Astrophys.* **529**, A75 (2011).
59. Brooks, S., Giudici, P. & Philippe, A. Nonparametric convergence assessment for MCMC model selection. *J. Comput. Graph. Stat.* **12**, 1–22 (2003).
60. Santerne, A. et al. SOPHIE velocimetry of Kepler transit candidates—XII. KOI-1257 b: a highly eccentric three-month period transiting exoplanet. *Astron. Astrophys.* **571**, A37 (2014).

61. Bayliss, D. et al. EPIC 201702477b: a transiting brown dwarf from K2 in a 41 day orbit. *Astron. J.* **153**, 15 (2016).
62. Osborn, H. et al. K2-110 b: a massive mini-Neptune exoplanet. *Astron. Astrophys.* **604**, A19 (2017).
63. Hatzes, A. P. et al. The mass of CoRoT-7b. *Astrophys. J.* **743**, 75 (2011).
64. Haywood, R. et al. Planets and stellar activity: hide and seek in the CoRoT-7 system. *Mon. Not. R. Astron. Soc.* **443**, 2517–2531 (2014).
65. Anglada-Escudé, G. & Tuomi, M. Comment on 'stellar activity masquerading as planets in the habitable zone of the M dwarf Gliese 581'. *Science* **347**, 1080 (2015).
66. Lissauer, J. J. et al. Validation of Kepler's multiple planet candidates. II. Refined statistical framework and descriptions of systems of special interest. *Astrophys. J.* **784**, 44 (2014).
67. Sotin, C., Grasset, O. & Mocquet, A. Mass–radius curve for extrasolar Earth-like planets and ocean planets. *Icarus* **191**, 337–351 (2007).
68. Badro, J., Côté, A. S. & Brodholt, J. P. A seismologically consistent compositional model of Earth's core. *Proc. Natl Acad. Sci. USA* **111**, 7542–7545 (2014).
69. Lebrun, T. et al. Thermal evolution of an early magma ocean in interaction with the atmosphere. *J. Geophys. Res.: Planets* **118**, 1155–1176 (2013).
70. Lodders, K. in *Principles and Perspectives in Cosmochemistry* (eds Goswami, A. & Reddy, B.) 379–417 (Astrophysics and Space Science Proc., Springer, Berlin, Germany, 2010).
71. Allègre, C. J., Poirier, J.-P., Humler, E. & Hofmann, A. W. The chemical composition of the Earth. *Earth. Planet. Sci. Lett.* **134**, 515–526 (1995).
72. Grevesse, N., Asplund, M. & Sauval, A. The solar chemical composition. *Space. Sci. Rev.* **130**, 105–114 (2007).
73. Asplund, M., Grevesse, N., Sauval, A. J. & Scott, P. The chemical composition of the Sun. *Annu. Rev. Astron. Astrophys.* **47**, 481–522 (2009).
74. Owen, J. E. & Jackson, A. P. Planetary evaporation by UV and X-ray radiation: basic hydrodynamics. *Mon. Not. R. Astron. Soc.* **425**, 2931–2947 (2012).
75. Pallavicini, R. et al. Relations among stellar X-ray emission observed from Einstein, stellar rotation and bolometric luminosity. *Astrophys. J.* **248**, 279–290 (1981).
76. Ochsenbein, F., Bauer, P. & Marcout, J. The VizieR database of astronomical catalogues. *Astron. Astrophys. Suppl. Ser.* **143**, 23–32 (2000).

Acknowledgements

We are grateful to the HARPS observers who conducted part of the visitor-mode observations at La Silla Observatory: R. I. Bustos, N. Astudillo, A. Wyttenbach, E. Linder, X. Bonfils, E. Hébrard and A. Suarez. A.S. thanks E. Hugot for comments on the manuscript. This publication is based on observations collected at the European Organisation for Astronomical Research in the Southern Hemisphere under ESO programme 198.C-0168. This publication makes use of The Data & Analysis Center for Exoplanets (DACE), which is a facility based at the University of Geneva (CH) dedicated to extrasolar planet data visualization, exchange and analysis. DACE is a platform of the Swiss National Centre of Competence in Research (NCCR) PlanetS, federating the Swiss expertise in exoplanet research. The DACE platform is available at https://dace.unige.ch. This research has made use of the NASA (National Aeronautics and Space Administration) Exoplanet Archive, which is operated by the California Institute of Technology, under contract with NASA under the Exoplanet Exploration Program. This research has made use of the VizieR catalogue access tool, CDS (http://vizier.u-strasbg.fr/vizier/surveys.htx). The original description of the VizieR service was published in ref. [76]. This publication makes use of data products from the Two-Micron All-Sky Survey, which is a joint project of the University of Massachusetts and the Infrared Processing and Analysis Center/California Institute of Technology, funded by NASA and the National Science Foundation. This publication makes use of data products from the Wide-field Infrared Survey Explorer, which is a joint project of the University of California, Los Angeles, and the Jet Propulsion Laboratory/California Institute of Technology, funded by NASA. The Porto group acknowledges support from Fundação para a Ciência e a Tecnologia (FCT) through national funds and from FEDER through COMPETE2020 by the grants UID/FIS/04434/2013 & POCI–01–0145-FEDER–007672, PTDC/FIS-AST/1526/2014 & POCI–01–0145-FEDER–016886 and PTDC/FIS-AST/7073/2014 & POCI-01-0145-FEDER-016880. FCT is further acknowledged through the Investigador FCT contracts IF/01312/2014/CP1215/CT0004 (S.C.C.B.), IF/00849/2015/CP1273/CT0003 (E.D.M.), IF/00650/2015/CP1273/CT0001 (V.A.), IF/01037/2013/CP1191/CT0001 (P.F.), IF/00169/2012/CP0150/CT0002 (N.C.S.) and IF/00028/2014/CP1215/CT0002 (S.G.S.) and for the fellowships SFRH/BD/93848/2013 (J.P.F.), PD/BD/128119/2016 (S.H.) and PD/BD/52700/2014 (J.J.N.), which are funded by FCT (Portugal) and POPH/FSE (EC). J.L.-B. acknowledges support from the Marie Curie Actions of the European Commission (FP7-COFUND). D.Bar. has been supported by the Spanish grant ESP2015-65712-C5-1-R. D.J.A. is funded under STFC consolidated grant reference ST/P000495/1. D.J.A.B. acknowledges support from the University of Warwick and the UKSA. E.F. is funded by the Qatar National Research Foundation (programme QNRF-NPRP-X-019-1). X.D. is grateful to the Society in Science–The Branco Weiss Fellowship for its financial support. R.L. thanks CNES for financial support through its postdoctoral programme. The project leading to this publication has received funding from Excellence Initiative of Aix-Marseille University–A*MIDEX, a French Investissements d'Avenir programme. The French group acknowledges financial support from the French Programme National de Planétologie (PNP, INSU). This work has been carried out in the frame of the NCCR PlanetS supported by the Swiss National Science Foundation (SNSF).

Author contributions

The Warwick group (D.J.A., D.J.A.B., A.D., F.F., E.F., J.J., G.K., J.K., K.W.F.L., T.L., J.McC., H.P.O., D.P.) detected the candidates. S.C.C.B., O.D. and M.D. reduced the POLAR–K2 light curves used in the candidate search. The Geneva group (D.Bay., F.B., R.F.D., X.D., H.Gi., C.L., F.P., S.U.) organized the HARPS runs, reduced the HARPS data and developed the DACE tool. A.S.B., S.G.S., D.J.A. and J.P.F. performed part of the visitor-mode runs on HARPS. M.H. derived the spectroscopic indices. V.A., E.D.M., N.C.S. and S.G.S. derived the stellar parameters and chemical composition of the star. J.L.-B. and D.Bar. performed the AstraLux observations and derived the background source confidence. H.Go. and A.S. performed the Bayesian analysis of the data with the PASTIS code that was initially developed by R.F.D., J.-M.A. and A.S. B.B., M.D., O.M. and A.A. developed the planet composition model and discussed the mantle evaporation. V.A., J.-M.A., D.Bar., S.C.C.B., D.Bay., I.B., A.S.B., F.B., D.J.A.B., M.D., E.D.M., O.D., J.P.F., P.F., H.Gi., G.H., S.H., R.L., C.L., J.J.N., H.P.O., F.P., D.P., N.C.S., S.G.S., S.U. and A.V. are co-investigators of the ESO–K2 large programme that is coordinated by A.S., who led the ESO proposal. A.S. led this study and wrote most of the manuscript. All authors contributed to the discussion of the paper.

Competing interests

The authors declare no competing interests.

Additional information

Supplementary information is available for this paper at https://doi.org/10.1038/s41550-018-0420-5.

Reprints and permissions information is available at www.nature.com/reprints.

Correspondence and requests for materials should be addressed to A.S.

Publisher's note: Springer Nature remains neutral with regard to jurisdictional claims in published maps and institutional affiliations.